

Fast fabrication of optical vortex generators by femtosecond laser ablation

Jian-Guan Hua¹, Zhen-Nan Tian^{1*}, Si-Jia Xu¹, Stefan Lundgaard^{2,3},
Saulius Juodkazis^{2,3*}

¹*State Key Laboratory of Integrated Optoelectronics, College of Electronic Science and Engineering, Jilin University, Changchun 130012, China*

²*Centre for Micro-Photonics, Faculty of Science, Engineering and Technology, Swinburne University of Technology, Hawthorn, VIC 3122, Australia*

³*Melbourne Centre for Nanofabrication, ANFF, 151 Wellington Road, Clayton, VIC 3168, Australia*

*Email: zhennan_tian@jlu.edu.cn, saulius.juodkazis@gmail.com

Abstract

Fast fabrication of micro-optical elements for generation of optical vortex beams based on the q -plate design is demonstrated by femtosecond (fs) laser ablation of gold film on glass. Q -plates with diameter of ~ 0.5 mm were made in ~ 1 min using galvanometric scanners with writing speed of 5 mm/s. Period of gratings of $0.8 \mu\text{m}$ and groove width of 250 nm were achieved using fs-laser ablation at $\lambda = 343$ nm wavelength. Phase and intensity analysis of optical vortex generators was carried out at 633 nm wavelength and confirmed the designed performance. Efficiency of spin-orbital conversion of the q -plates made by ablation of 50-nm-thick film of gold was $\sim 3\%$. Such gratings can withstand thermal annealing up to 800°C . They can be used as optical vortex generators using post-selection of polarisation.

Keywords: nanofabrication, ablation, q -plates, micro-optics, optical vortex

1. Introduction

Optical vortex generators which produce beams with a spiraling wavefront are used in laser structuring of materials and, recently, for polymerisation [1, 2]. Optical vortices can be generated using spatial light modulators

(SLMs) with encoded phase patterns upon reflection. However, for a practical use optical elements for the fixed topological charge, l , which defines the azimuthally spiraling phase $e^{il\theta}$ along the beam propagation are sought after for applications where orbital angular momentum (OAM) is harnessed. Miniaturisation of vortex generators is another trend [3] which empowers laser tweezer applications for trapping and manipulation of microscopic materials [4]. Micro-optical elements for optical vortex generation can be made using spiral plates, which are 3D structures and require 3D printing capability of high precision [5]. The spiral plates can reach 100% efficiency at zero reflection and absorption and transforms light into an optical vortex independent of the polarisation state of the incoming light. Among other methods to generate optical vortex, the spin-orbital elements which perform spin, σ to orbital, l , conversion defines a prominent family. The spin and orbital angular momentum (SAM, OAM) defines the total angular momentum $j = \sigma + l$ by the two independent contributions which can be engineered independently. The form-birefringent patterns whose slow-optical axis has a local angular orientation $\theta = q\alpha$ defined by the azimuthal angle α , where q is the half-integer, hence, the q -plates [6, 7, 8]. Q -plates are used to generate beams which carry OAM $l = 2q$ and can be realised using optically anisotropic materials: liquid crystals, semiconductors, silica glass, and different design of metallic or dielectric metasurfaces [6, 9, 10, 11, 12, 13, 14, 15]. However, one of the most practical solutions of q -plate fabrication by alignment of liquid crystals on a mechanically rubbed surface can only deliver resolution of $\sim 10 \mu\text{m}$.

Direct laser printing of q -plates for a typical wavelength of $1.5 \mu\text{m}$ used in telecommunications and shorter visible wavelengths is a challenging task due to required high aspect ratio grating patterns with duty cycle of 0.5 (grating period is twice as large as the width of the polymer log in the grating) [16]. Despite a low efficiency of transmission through nano-grooves made in an optically opaque 50-100 nm thick metal film, the purity (see Sec. 2.1) of optical vortex generation is very high as defined by portion of the circularly polarised photons which switch their polarisation (spin, σ) and acquire OAM, $l \neq 0$ [17, 18]. It is of a practical relevance to explore possibility of a fast laser fabrication [19, 20, 21, 22] of binary q -plates by ablation of grooves in metal as compared with more complex material structuring through established nano-lithography and plasma etching for high efficiency and purity optical vortex generators [23].

Here, fabrication of q -plates by ablation of gold film is demonstrated with

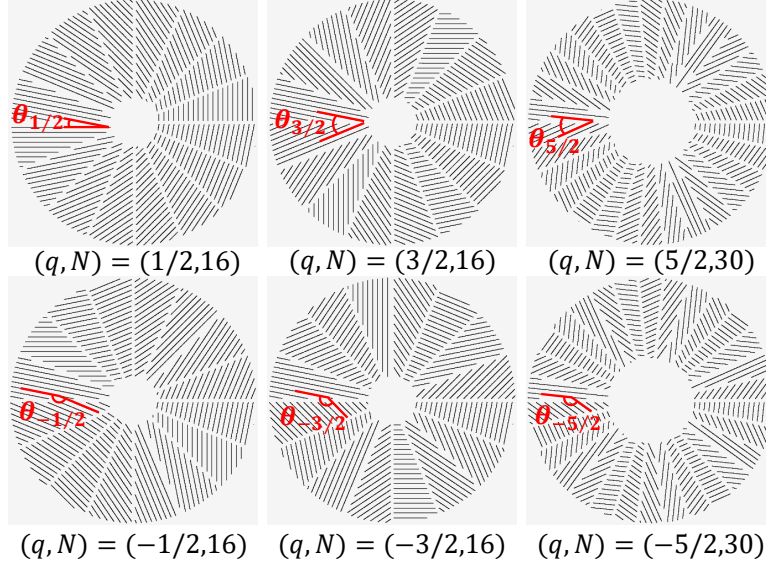


Figure 1: Design of q -plates of different q numbers; q values are changing in half-integer steps and can have \pm sign. The number of segments was N . These design files with periods of gratings $\Lambda = 0.4; 0.8 \mu\text{m}$ were prepared for xy -scanners.

fast writing capability taking only 1 min per element made on a 0.5 mm diameter area. Phase and intensity patterns of the binary q -plates confirmed optical vortex generation at 633 nm wavelength.

2. Experimental: samples and procedures

2.1. Q -plates: definitions

The scalar vortex beams are solutions of Helmholtz equation and are defined by the Laguerre-Gaussian (LG) modes [24]:

$$E_0^l(r, \theta, z) = \sqrt{\frac{2}{2\pi l!}} (\sqrt{2}r/w(z))^l (2r^2/w(z)^2) L_0^l e^{i\theta} e^{-ikr^2/2q(z)} e^{i\psi}, \quad (1)$$

where $k = 2\pi/\lambda$ is the wavevector, $\psi(z) = (l + 1) \tan^{-1}(z/z_R)$ is the Gouy phase, $q(z) = \pi R(z)w(z)^2/\pi w(z)^2 - iR(z)\lambda$ is the complex beam parameter, $R(z) = z[1+(z_R/z)]$ is the evolving curvature radius, $w(z) = w_0\sqrt{1+(z/z_R)^2}$ is the evolving beam width, $z_R = \pi w_0^2/\lambda$ is the Rayleigh lengths, and L_0^l is the Laguerre polynomials.

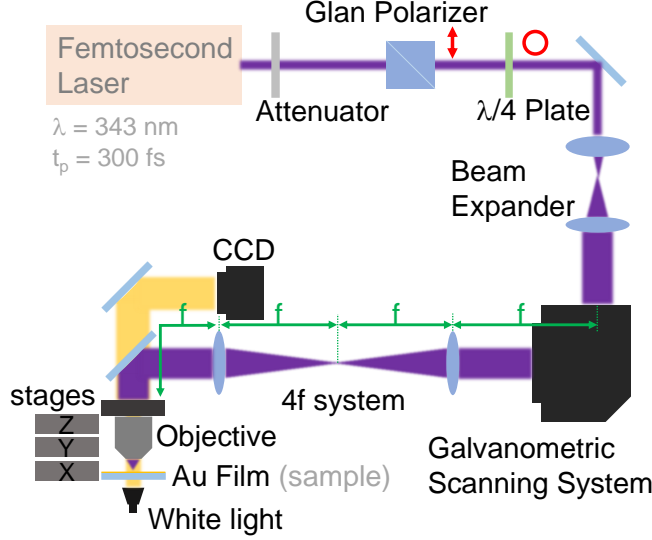


Figure 2: Fs-laser fabrication setup which used Schwarzschild reflection objective lens of numerical aperture $NA = 0.5$.

Q-plates made of grating structures that have an orientation distribution $\theta(x, y) = q\alpha$, where the azimuthal angle $\alpha = \tan^{-1}(y/x)$ defined in Cartesian coordinates were fabricated. The emerging electric field, \mathbf{E}_{out} , after passing through the q-plate is given [18]:

$$\mathbf{E}_{out} = \mathbf{E}_{in}\tau[\cos(\Delta/2)\mathbf{e}_{\sigma} + i\sin(\Delta/2)e^{i2\sigma q\alpha}\mathbf{e}_{-\sigma}], \quad (2)$$

where $\Delta = \Delta' + i\Delta''$ with $\Delta^{(', '')} = k[n_{\parallel}^{(', '')} - n_{\perp}^{(', '')}]h$ are defining the retardance Δ' and dichroism Δ'' for the h height of q-plate (along the light propagation length) at wavevector $k = 2\pi/\lambda$ for wavelength λ , and $\tau = e^{-k(n_{\parallel}'' + n_{\perp}'')h/2}$ is transmittance which accounts for losses and defines the efficiency of the spin-orbital coupling. The incident field is circularly polarised $\mathbf{E}_{in} \propto \mathbf{e}_{\sigma=\pm 1}$ with $\mathbf{e}_{\sigma} = \frac{1}{\sqrt{2}}(\mathbf{x} + i\sigma\mathbf{y})$ and $\sigma = \pm 1$ defining the left and right-handed polarisations in the Cartesian frame, respectively. The spin-orbital coupling efficiency is determined by the dichroism and birefringence properties of the material and is maximised for the half-wavelength condition of the q-plate: $\Delta' = \pi$ modulo 2π .

The purity of optical vortex generation $\eta = |\mathbf{E}_{out} \cdot \mathbf{e}_{\sigma}|^2 / |\mathbf{E}_{out}|^2 = \sin^2(\Delta'/2)$ defines the relative weight of the circularly polarised output field component

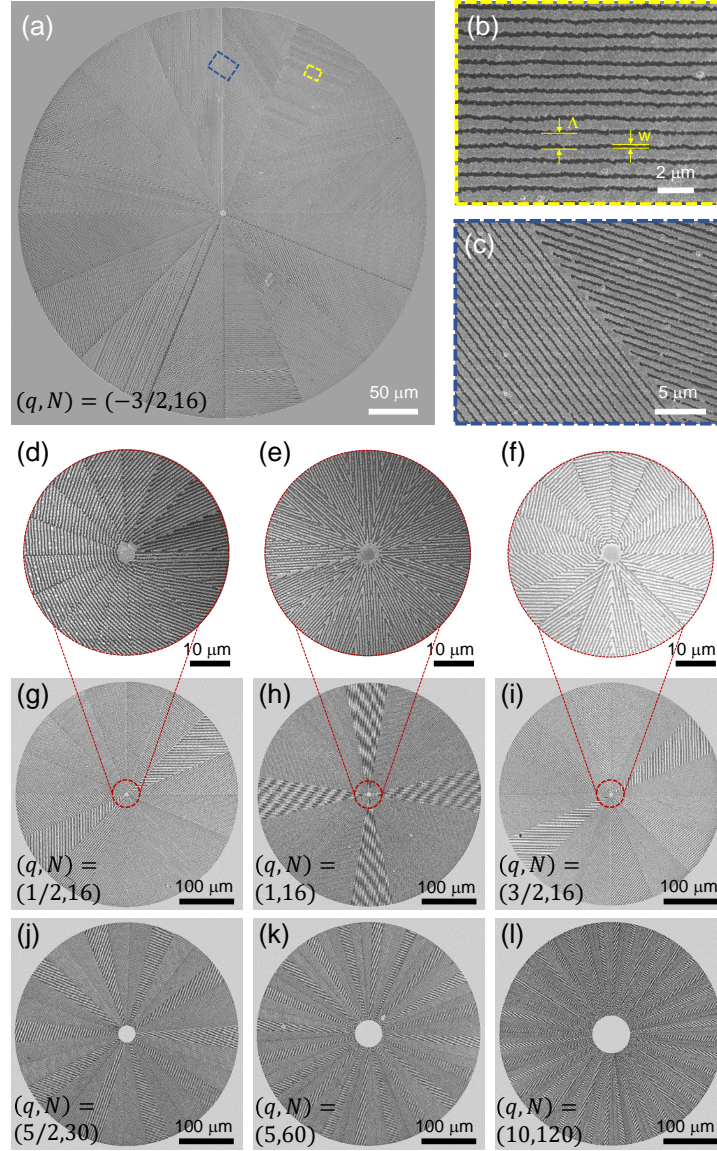


Figure 3: (a) SEM image of an $q = -3/2$ plane made of $N = 16$ azimuthally arranged grating segments ablated on 50-nm-thick Au film on glass. (b,c) Magnified SEM images of the two regions marked in (a). The period of grating was $\Lambda = 800$ nm and the ablated line width $w \approx 250$ nm. (d-l) SEM images of ablated q -plates with different q values. (a-c) Magnified images of selected q -plates.

carrying the optical vortex [18]. When optical losses are present due to dichroism, the purity is given as [25]:

$$\eta = \frac{1}{2} \left[1 - \frac{\cos \Delta'}{\cosh \Delta''} \right]. \quad (3)$$

At the half-waveplate condition $\Delta' = \pi$, $\eta = 1$ when dichroic losses are absent $\Delta'' = 0$. Dichroic losses are measured for the $q = 0$ plate (a grating) for two linearly polarised beam orientations are $\tau \equiv e^{-\Delta''} = \sqrt{P_{\parallel}/P_{\perp}}$. This defines limitation for the achievable purity from the material point of view. Experimentally measured purity is the power of the optical vortex component with $l \neq 0$ to the total transmitted power through the q -plate (the total transmission through the 50-nm-thick Au film was smaller than 0.8% at all visible wavelengths, see, Sec. Appendix A).

Thin binary transmission masks have weak birefringence [26] and low transmission, hence, the efficiency of vortex generation are expected to be low. The retardance is defined by a phase shift between TE and TM modes through the thin film (50 nm in our case) [26]. The pair (Δ', Δ'') is defining the purity (Eqn. 3). The dichroic ratio used to characterise grid polarisers $D_r = A_{\parallel}/A_{\perp}$ defined by the absorbance of E-field \parallel to the grid (high A) and that perpendicular \perp (low A) is directly related to the dichroic losses Δ'' . When $D_r = 1$ there is no anisotropy of absorbance (also transmittance, T).

Q-plate patterns were designed for control of a laser fabrication software (Fig. 1). The number of segments, N were maximised to obtain the most efficient addition of light emerging through the grating slits. For the large q values the central part of the element was not structured, when there was less than one period fitting into the segment section at small radius. For the sake of fabrication flexibility, q -plates with different q signs \pm were fabricated (Fig. 1). For the actual applications, the sign of vortex beam (OAM l) can be changed by changing the sign of the incoming SAM σ .

2.2. Fabrication and characterisation

Q-plates were fabricated by ablation of a 50-nm-thick gold film deposited on fused silica substrates (Jinlong photoelectric, Ltd.) by magnetron sputtering; a few nanometers Cr adhesion layer was used between Au and silica. Figure 2 shows setup used for laser fabrication. It is based on a Yb:KGW solid state fs-laser (Pharos, Light Conversion Ltd.), galvo-scanners (Sunny Technology Ltd.), and reflection-type Schwarzschild objective lens of numerical aperture $NA = 0.5$ (Thorlabs, LMM-40X-UVV).

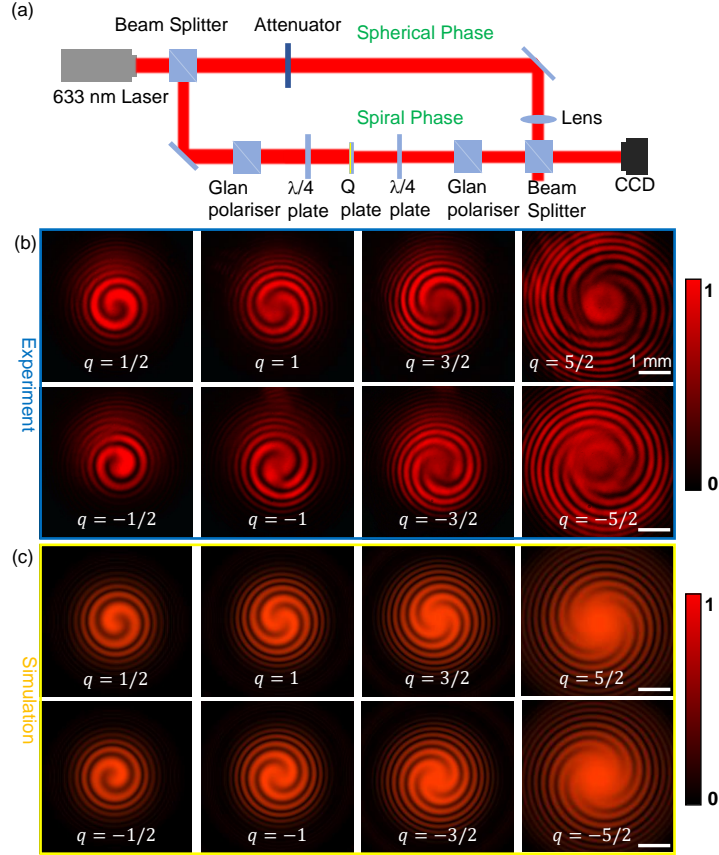


Figure 4: (a) A phase characterisation setup of the optical vortex beams generated by q -plates. (b) Experimental interferograms of different q -plates. Scale bars 1 mm. (c) Numerical simulations of the phase of the corresponding LG vortex beams (Eqn. 1).

A high 200 kHz repetition rate fs-laser at $\lambda = 343$ nm wavelength was obtained via an internally integrated triple frequency system (Pharos). The shorter wavelength was used to achieve higher machining resolution. The high repetition enables higher processing speeds and improves processing efficiency. The pulse width of the fs-laser was $t_p = 300$ fs. First, the laser passes through the Glan prism and the $\lambda/4$ plate to generate a circular polarization in order to avoid the influence of polarization under high numerical aperture focusing on the spot shape and reduce effects related to directionality of electronic heat diffusion depending on the scanning direction [27]. The laser then passes through a $3\times$ beam expander system to obtain a larger

spot size and is guided through the galvanometric xy-scanners, which can deliver a high scanning speed of 5 mm/s (on sample) used in this study. Rapid movement of the focal spot was key to processing efficiency. An internal laser shutter was used for blocking the beam during a change of location required by the drawing algorithm. The 4f optical system consisting of a double lens was implemented for transferring of the deflection angle of the galvanometric scanners onto the objective entrance. We also used a high numerical aperture UV transmissive objective (Nikon, 20 \times magnification, $NA = 0.75$) which had 60% transmittance at the 343 nm wavelength. The laser power measured before the entrance to the objective lens was 1.1 mW (or pulse energy $E_p = 3.3$ nJ/pulse on the sample).

Interestingly, the Schwarzschild objective lens was delivering a better quality lines at the end points. The diameter of the focal spot was $d = 1.22\lambda/NA = 837$ nm. Ablation was carried out at $E_p = 4$ nJ/pulse (at objective transmission of $T = 33\%$ at $\lambda = 343$ nm), at repetition rate of 200 kHz and at $NA = 0.5$ focusing. This corresponds to the fluence per pulse of $F_p = E_p/[\pi(d/2)^2] = 0.24$ J/cm² and is close to the threshold of ablation of metals and the average irradiance was $I_p = F_p/t_p = 0.8$ TW/cm². The laser ablation features smaller than the diffraction limit at the used focusing $\frac{d}{2} = 418$ nm can be printed on the surface by ablation due to the threshold effect as it was the case in this study. Laser ablated patterns were characterised using scanning electron microscopy (SEM, Jeol JSM-7500F).

For numerical modeling of the phase and intensity of the vortex beams we used Virtual Lab Fusion (LightTrans) software.

3. Results and Discussion

Laser ablated pattern of $q = -3/2$ plate composed of $N = 16$ grating segments is shown in Fig. 3. The period $\Lambda = 0.8$ μm with opening of groove $w \approx 250$ nm was fabricated in 43 s. The diameter of the q -plate was 0.4 mm. Close proximity of the segments with separation ~ 1 μm was achieved with high fidelity (Fig. 3)(c)) without widening of the lines at the end point of a scan lines. Even periods of $\Lambda = 0.4$ μm were achieved with a similar ablated groove width. Flexibility of this approach is summarised in Fig. 3(d-1) showing different patterns reaching the demanding $q = 10$ and $N = 120$ conditions. The most complex q -plates attempted took only approximately 2.5 \times longer as compared with the simplest ones. The same resolution of fabrication was achieved for the most complex patterns at the writing/printing

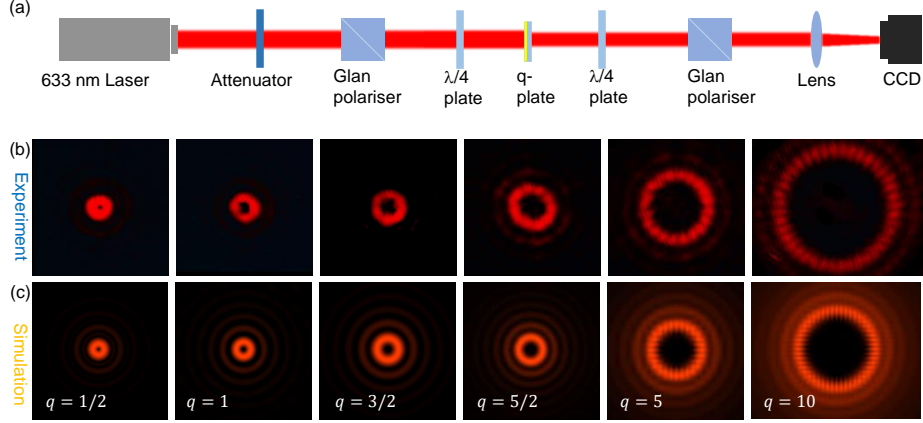


Figure 5: (a) Setup for intensity readout of the optical vortex beams generated by q -plates. (b) Experimental readout of intensity from different q -plates. (c) Numerical simulations of the intensity of the corresponding LG vortex beams (Eqn. 1).

speed used in this study.

To check the property of optical vortex generation, the spiraling phase was revealed using two arms interferometer (Fig. 4(a)). The used 633 nm wavelength had only 0.22% transmission through the unstructured Au film (Sec. Appendix A, Fig. A.1). A good qualitative match between the experimental interferograms and calculated by Virtual Lab Fusion (LightTrans) was corroborated. The vortex beam size and phase structure were following that expected from design parameters of q -plate.

For optical characterisation, polarisation state was controlled in the interferometer. The second $\lambda/4$ plate (Fig. 4(a)) was set at $\pi/2$ to the first one (before the q -plate). With this setting, the circularly polarised beam with $+\sigma$ and $l = 0$ (a plane wave before the q -plate) becomes linearly polarised and the second Glan polariser is at the crossed orientation to the incoming polarisation. The vortex beam generated via spin-orbital coupling has emerging photons with $l \neq 0$ with opposite spin $-\sigma$ which are transmitted through the second Glan polariser. In the reference arm, an attenuator and a lens were added to obtain the best contrast of the interferogram of the two beams with spherical wavefronts. A qualitative match with the experimentally observed interference patterns was obtained numerically using Laguerre-Gauss (LG) beams (Eqn. 1) interference with a Gaussian intensity envelope (Fig. 4(c)).

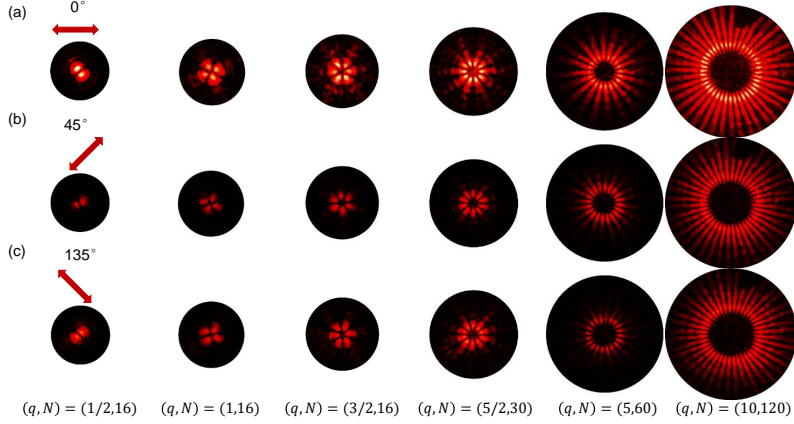


Figure 6: Intensity readout of different q -plates with linearly polarised beam at: 0° (a), 45° (b) and 135° (c). The segment of q -plate which is rotated at 45° to the incident polarisation is contributing the largest intensity.

The efficiency of the spin-orbital conversion was tested by measuring power after the second Glan polariser at two orthogonal orientations of the low and high transmittance and the value of 3.1% was determined as power of the $l \neq 0$ mode to the total power [17] (see, Sec. A.2 for determination of optical slit retardance which defines Δ'). It is comparable with purely dielectric polymerised q -plates [16]. All dielectric q -plates with duty cycle of 0.5 can potentially reach high efficiency and purity (Eqns. 2, 3) of optical vortex generation, but it is very demanding to satisfy the required effective structure height for the π phase retardance for an effectively lower mass density pattern. Moreover, the laser printing throughput for sub-1 mm areas will take up to 10^3 times longer even for $\sim 1 \mu\text{m}$ -tall q -plates as in ref. [16].

To determine the dichroic ratio D_r a grating ($q = 0$ plate) was fabricated over the 0.4-mm-diameter area and transmission of a linearly polarised light perpendicular (T_{max}) and parallel (T_{min}) to the grating wires was measured $D_r = \lg(T_{min})/\lg(T_{max}) = 1.32$; for a grating $D_r > 1$ it is expected. The dichroism estimated from ratio of transmitted powers was $\Delta'' = 0.04$. Transmission through a $q = 1/2$ plate was measured using a reference, an ablated 0.4-mm-diameter hole in Au, and was 76.6%. A slightly lower transmission is expected for larger q values due to increasing central region of unstructured q -plate.

Thermal stability of a high resolution q -plate pattern was tested next. High temperature annealing at 830°C for 40 min was able to reduce random

pattern of debris nanoparticles generated by ablation (See Sec. Appendix A). This marginally improved transmission and would need a dedicated study of thermal treatment effects on different thickness gold films, grating period and duty cycle. Importantly, the thermal test also shows that the fabricated q -plates can withstand high irradiance conditions and will not deteriorate in the high power laser beam due to a comparatively lower transmission compared with dielectric q -plates. Good adhesion and thermal stability of Au film on silica can be harnessed for a hard mask in Ar plasma etching. This can increase the retardance of the structure linked to Δ' and the purity of the optical vortex generation and will be investigated in future.

Geometry of the generated vortex beams and uniformity of fabricated segments were further investigated by direct imaging of the intensity distribution. The intensity readout of the optical vortex beam shows the doughnut shape (Fig. 5) with the peak intensity position defined by the radius $r = w_0\sqrt{l}/2$, where w_0 is the waist of the Gaussian TEM₀₀ mode. Using a circularly polarised illumination of the q -plate the intensity distribution after a compensating $\lambda/4$ plate is shown in (b) for the $l \neq 0$ vortex beam portion.

The fabricated q -plates are composed out of grating segments and their position in the optical element can be visualised using linearly polarised light illumination as shown in Fig. 6. When orientation of the grating was at $\pi/4$ with respect to the linear polarisation of the illuminating beam, the strongest intensity was observed due to the form birefringence. The number of bright lobes was $4q$; a typical Maltese cross like pattern is observed for the radial orientation pattern of $q = 1$. Uniformity of side lobes is testimonial for the same ablation pattern quality among the segments of q -plate.

4. Conclusions

Fast ~ 1 min fabrication of ~ 0.5 mm diameter q -plates of different complexity is demonstrated with resolution of 250 nm grooves and period of 800 nm on gold coated silica. This simple binary grating design delivered a 3.1% efficiency of the spin-to-orbital conversion. The quality of the optical doughnut beam intensity and phase patterns were corroborated using interferometry. By using post-selection polarisation optics (as used in beam characterisation in this study), vortex generators can be delivered. They could withstand high laser powers and light induced heating as can be inferred from the thermal treatment of the q -plates. Linear scan speeds were reaching 5 mm/s with pulse to pulse shift by 25 nm at 200 kHz repetition

rate (or 33.5 pulses per $1.22\lambda/NA = 0.84 \mu\text{m}$ diameter focal spot) and ablated 250-nm-wide lines in a 50-nm-thick gold film. As it was established earlier, such optical vortex generators have optical broadband “white” performance [18]. A more efficient vortex beam generation and a higher purity of spin-orbital conversion can be envisaged after a plasma etching using the ablated q -plate pattern as a hard mask.

References

References

- [1] J. Ni, C. Wang, C. Zhang, Y. Hu, L. Yang, Z. Lao, B. Xu, J. Li, D. Wu, J. Chu, Three-dimensional chiral microstructures fabricated by structured optical vortices in isotropic material, *Light: Sci. Appl.* 6 (2017) e17011.
- [2] J. Lee, Y. Arita, S. Toyoshima, K. Miyamoto, P. Panagiotopoulos, E. M. Wright, K. Dholakia, T. Omatsu, Photopolymerization with Light Fields Possessing Orbital Angular Momentum: Generation of Helical Microfibers, *ACS Photonics*, 5 (2018) 4156.
- [3] E. Brasselet, N. Murazawa, H. Misawa, S. Juodkazis, Optical vortices from liquid crystal droplets, *Phys. Rev. Lett.* 103 (2009) 103903.
- [4] H. Misawa and S. Juodkazis, Photophysics and photochemistry of a laser manipulated microparticle, *Prog. Polym. Sci.* 24 (1999) 665.
- [5] E. Brasselet, M. Malinauskas, A. Žukauskas, S. Juodkazis, Photopolymerized microscopic vortex beam generators : precise delivery of optical orbital angular momentum, *Appl. Phys. Lett.* 97 (2010) 211108.
- [6] G. Biener, A. Niv, V. Kleiner, E. Hasman, Formation of helical beams by use of Pancharatnam - Berry phase optical elements, *Opt. Lett.* 27 (2002) 1875 – 1877.
- [7] L. Marrucci, C. Manzo, D. Paparo, Optical spin-to-orbital angular momentum conversion in inhomogeneous anisotropic media, *Phys. Rev. Lett.* 96 (2006) 163905.

- [8] S. Slussarenko, A. Murauski, T. Du, V. Chigrinov, L. Marrucci, E. Santamato, Tunable liquid crystal q-plates with arbitrary topological charge, *Opt. Express* 19 (5) (2011) 4085–4090.
- [9] Y. Shimotsuma, P. G. Kazansky, J. Qiu, K. Hirao, Self-organized nanogratings in glass irradiated by ultrashort light pulses, *Phys. Rev. Lett.* 91 (2003) 247405.
- [10] E. Karimi, S. A. Schulz, I. De Leon, H. Qassim, J. Upham, R. W. Boyd, Generating optical orbital angular momentum at visible wavelengths using a plasmonic metasurface, *Light Sci Appl* 3 (5) (2014) 4.
- [11] G. Li, M. Kang, S. Chen, S. Zhang, E. Y.-B. Pun, K. W. Cheah, J. Li, Spin-enabled plasmonic metasurfaces for manipulating orbital angular momentum of light, *Nano Lett* 13 (9) (2013) 4148–4151.
- [12] J. Jin, J. Luo, X. Zhang, H. Gao, X. Li, M. Pu, P. Gao, Z. Zhao, X. Luo, Generation and detection of orbital angular momentum via metasurface, *Sci. Reports* 6 (2016) 24286.
- [13] R. C. Devlin, A. Ambrosio, D. Wintz, S. L. Oscurato, Z. A. Yutong, M. Khorasaninejad, J. Oh, P. Maddalena, F. Capasso, Spin-to-orbital angular momentum conversion in dielectric metasurfaces, e-prints ArXiv :1605.03899 (2016)
- [14] S. Kruk, B. Hopkins, I. I. Kravchenko, A. Miroshnichenko, D. N. Neshev, Y. S. Kivshar, nvited article: Broadband highly efficient dielectric metadevices for polarization control, *Appl. Phys. Lett.: Photonics* 1 (2016) 030801.
- [15] S. M. Kamali, E. Arbabi, A. Arbabi, Y. Horie, A. Faraon, Highly tunable elastic dielectric metasurface lenses, *Laser Photn. Rev.* 10 (2016)
- [16] X. Wang, A. A. Kuchmizhak, E. Brasselet, S. Juodkazis, Dielectric geometric phase optical elements fabricated by femtosecond direct laser writing in photoresists, *Appl. Phys. Lett.* 110 (18) (2017) 181101.
- [17] E. Brasselet, G. Gervinskas, G. Seniutinas, S. Juodkazis, Topological shaping of light by closed-path nanoslits, *Phys. Rev. Lett.* 111 (19) (2013) 193901.

- [18] D. Hakobyan, H. Magallanes, G. Seniutinas, S. Juodkazis, E. Brasselet, Tailoring orbital angular momentum of light in the visible domain with metallic metasurfaces, *Adv. Opt. Mater.* 4 (2016) 306 – 312.
- [19] Y.-L. Zhang, Q.-D. Chen, H. Xia, H.-B. Sun, Designable 3D nanofabrication by femtosecond laser direct writing, *Nano Today* 5 (2010) 435 – 448.
- [20] H. Xia, J. Wang, Y. Tian, Q.-D. C. X.-B. Du, Y.-L. Zhang, Y. He, H.-B. Sun, Ferrofluids for fabrication of remotely controllable micro-nanomachines by two-photon polymerization, *Adv. Mat.* (22) 3204 – 3207.
- [21] Y. Zhang, L. Guo, S. Wei, Y. He, H. Xia, Q.-D. Chen, H.-B. Sun, F.-S. Xiao, Direct imprinting of microcircuits on graphene oxides film by femtosecond laser reduction, *Nano Today* 5 (2010) 15 – 20.
- [22] L. Wang, Q.-D. Chen, X.-W. Cao, R. Buividas, X. Wang, S. Juodkazis, H.-B. Sun, Plasmonic nano-printing: large-area nanoscale energy deposition for efficient surface texturing, *Light: Sci. Appl.* 6 (2017) e17112.
- [23] G. Seniutinas, E. Brasselet, A. Balcytis, C. David, S. Juodkazis, Diamond: a gem for micro-optics, *Materials Today* (2018) (in press).
- [24] L. Allen, M. W. Beijersbergen, R. J. C. Spreeuw, J. P. Woerdman, Orbital angular momentum of light and the transformation of Laguerre-Gaussian laser modes, *Phys. Rev. A* 45 (11) (1992) 8185 – 8189.
- [25] D. Hakobyan, Spin-orbit optomechanics of space-variant birefringent media, Ph.D. thesis, University of Bordeaux and Swinburne University of Technology (2016).
- [26] K. Iwami, M. Ishii, Y. Kuramochi, K. Ida, N. Umeda, Ultrasmall radial polarizer array based on patterned plasmonic nanoslits, *Appl. Phys. Lett.* 101 (2012) 161119.
- [27] S. Rekštytė, T. Jonavicius, D. Gailevičius, M. Malinauskas, V. Mizeikis, E. G. Gamaly, S. Juodkazis, Nanoscale precision of 3D polymerisation via polarisation control, *Adv. Opt. Mat.* 4 (8) (2016) 1209 – 1214.

Acknowledgements

The authors thank the support of the National Key R&D Program of China (No.2017YFB1104600) and the National Natural Science Foundation of China (NSFC) 61590930, 61522503, 51335008, and 61435005. SJ is also grateful for the ChangJiang scholar project at Jilin University and partial support via DP170100131 grant. We acknowledge discussion on properties of optical vortex beams with Etienne Brasselet.

Appendix A. Supplement

Figure A.1 shows transmission spectrum of the unstructured 50-nm-thick gold film on silica. At the used 633 nm wavelength used to characterise q -plates transmission was very low 0.22%. At the Au plasmonic peak of gold ~ 500 nm the background transmission can be up to $2.5\times$ higher, however, even then it is below 1%.

Figure A.3 shows structural changes of the gold ablated film after sequential annealing at higher temperatures.

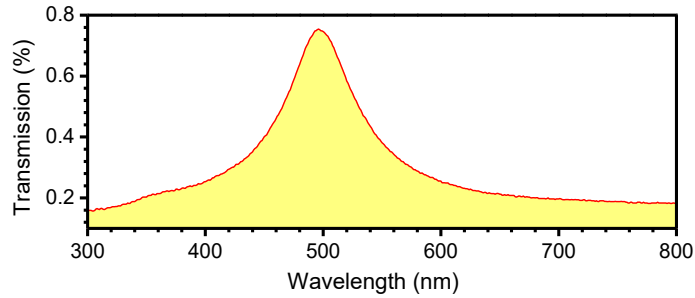


Figure A.1: Transmission spectrum of the used 50-nm-thick Au film use for laser inscription of the q -plates.

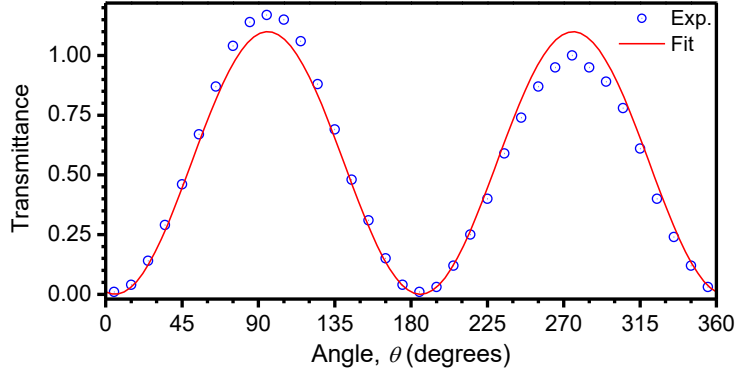


Figure A.2: Transmission of the linearly polarised 633 nm light through an ablated grating in a Au film ($q = 0$ plate of 0.4 mm diameter) at different angles, θ , of the linear analyser (setup adapted from Fig. 5(a)). Fit was made with a function proportional to the Stokes parameter $S_0 = \frac{1}{4}[1 + \cos(\Delta^\circ - 2(90^\circ + \theta))]$ [26]. The best fit was achieved for the retardance (in degrees) $\Delta^\circ = (11 \pm 2)^\circ$ or 3.1% of the wavelength, or $\Delta nd = 19.3$ nm. The thickness of Au film was $d = 50$ nm; hence $\Delta n = 0.39$. Refractive index of gold $n + i\kappa = 0.18344 + i3.4332$ at 633 nm.

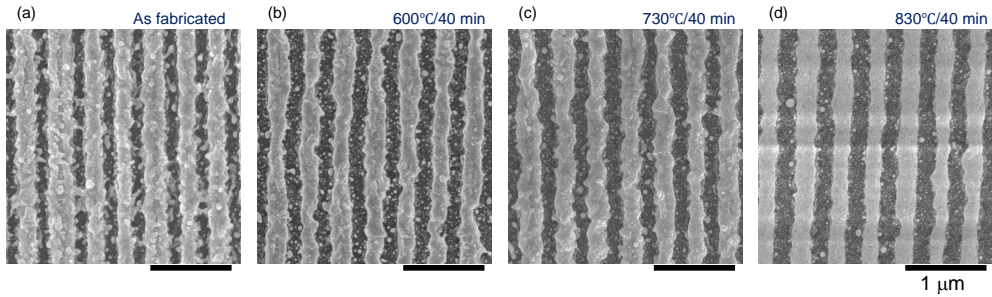


Figure A.3: Structural changes of Au-on-silica patterns induced by sequential annealing at high temperatures. Ablation was carried out by 343 nm/300 fs pulses.